Computers and Geotechnics 165 (2024) 105860

Contents lists available at ScienceDirect

Computers and Geotechnics

journal homepage: www.elsevier.com/locate/compgeo

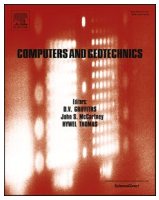

# Root size effects on transverse root-soil interactions

X. Zhang [a,b], J.A. Knappett [c,*], M.O. Ciantia [c,g], A.K. Leung [b,d], H. Wang [b,e], T. Liang [b,f]

[a] Department of Civil and Airport Engineering, Nanjing University of Aeronautics and Astronautics, Liyang, China
[b] Formerly University of Dundee, Dundee, UK
[c] University of Dundee, Dundee, UK
[d] Hong Kong University of Science and Technology, Hong Kong SAR, China
[e] Ziyang Hi-Tech Industrial Zone Management Committee, Ziyang, China
[f] Center for Hypergravity Experimental and Interdisciplinary Research, Zhejiang University, Hangzhou, China
[g] Universita' Degli Studi di Milano Bicocca, Milan, Italy

ARTICLE INFO

*Keywords:*
Vegetation
Root-soil interaction
Distinct Element Method
Size effects
Sand

ABSTRACT

For smaller lateral plant roots in coarse-grained soils, a potentially large relative size of soil particles compared to the roots may affect their transverse resistance. Even for the larger roots of trees, particle size effects may be important, e.g. when testing 1:*N* reduced scale models in a geotechnical centrifuge. The Discrete Element Method (DEM) was used to investigate this problem. A rigid lateral root segment under transverse loading in plane strain was simulated and compared with Finite Element Method (FEM) simulations, where the soil was modelled as a continuum (no particle size effects). Even at the lower root/particle diameter ratios ($d_r/D_{50}$) investigated (6 to 21), particle size effects on transverse capacity were negligible upon push-in, while during uplift, they were observed for $d_r/D_{50} < 8$, arising from the dimension of the uplifted soil volume above the root. The material properties of roots are also typically diameter dependent. Further simulations of long flexible roots subject to end rotation were performed employing a beam-on-non-linear-Winkler-foundation approach, using *p-y* curves obtained from the DEM or FEM simulations. Compared with particle-size related effects, diameter-dependent variation of material properties had a much larger controlling effect on root capacity and stiffness as relevant for plant/tree overturning.

## 1. Introduction

Plant roots are natural soil anchors which could play a prominent and sustainable role in risk mitigation strategies for geotechnical infrastructure (e.g. as a nature-based solution, NBS) through modifying the groundwater regime (Smethurst et al. 2012) and/or through direct mechanical soil strength improvement (Stokes et al. 2009; Karimzadeh et al. 2021, 2022). Given that landslides, debris flows and windstorms are common hazards that can cause ecosystem degradation and vegetation destruction (McCarthy et al. 2010; Cui et al. 2012; Zhang et al. 2023), understanding root-soil interaction behaviour under transverse loads has long been of interest in forestry. It is also of interest in Civil Engineering, e.g. trees could provide protection against earthquake-induced landslides (Liang et al. 2015) and windthrown trees in slopes may be a trigger for landslides (Jakob and Lambert 2009).

An increasing body of research has used scaled (1: *N*) root models to systematically investigate root-soil mechanical interactions in the laboratory, either under 1 ***g*** conditions (Mickovski et al. 2010; Harnas et al. 2016; Zhang et al. 2018) or at elevated gravity within a geotechnical centrifuge (Liang et al. 2015; Zhang et al. 2023). Compared with field winching (pulling) tests of trees or field shearbox tests, key variables (e.g. model root properties, root architecture, soil properties, groundwater conditions and loading conditions) in these ***N-g*** tests can be closely controlled. However, scale effects related to particle size may exist (Liang and Knappett 2017) in case of over-scaling of the root model, where the surrounding soil can no longer be considered as a continuum, especially for coarse granular soils. Even for root-soil interactions at 1:1 (full) scale in the laboratory or in the field, roots with small diameter (compared with particle size) may similarly be subject to scale effects related to particle size in coarse-grained soils (e.g. gravels or granular tills). Based on centrifuge testing of foundations, existing studies have found that particle size effects depend on the shear band formation (Lehane and White 2005; Lehane et al. 2005; Athani et al. 2017), soil-structure interface roughness (Sinnreich 2011) and stress

* Corresponding author at: School of Science and Engineering, University of Dundee, Dundee, DD1 4HN. UK.
*E-mail address:* j.a.knappett@dundee.ac.uk (J.A. Knappett).

https://doi.org/10.1016/j.compgeo.2023.105860
Received 21 June 2023; Received in revised form 22 September 2023; Accepted 16 October 2023
Available online 24 October 2023

level (Bałachowski 2007). Garnier et al. (2007) suggested that the ratio of the diameter of shallow footing to particle size should be larger than 35 to avoid any particle size effects, whereas Ovesen (1981) reported no scale effects on uplift resistance of plates in loose and dense sand even with the ratio reduced to 25. Similarly, Palmer et al. (2003) found no significant particle size effects on the uplift resistance of buried pipelines at a threshold ratio of 80. However, compared with foundations and pipelines, plant roots could result in much lower structure-grain size ratios, which has been rarely investigated (e.g. Mickovski et al. 2010). Also, in contrast to conventional geotechnical structures, plant roots are normally located at very shallow depth, in which case the effect of low confining stress (and correspondingly high dilatancy) should also be considered.

Considering the tree overturning problem shown schematically in Fig. 1, under external lateral loading (e.g. from wind), individual lateral roots may be idealised to be either uplifted or pushed into the soil. The aim of this study is to first numerically simulate a rigid lateral root segment of such a root system under a plane strain condition, validating performance against physical model testing, and then using the model to investigate the influence, if any, of potential particle size effects that may arise at different $d_r/D_{50}$ ratios, e.g. 1:$N$ scale physical model tests of lateral roots of a particular prototype. For a higher $N$, chosen to avoid boundary effects in designing such tests, the model roots become smaller while the soil particle size remains the same; this changes the ratio of root diameter ($d_r$) to mean particle size ($D_{50}$) under the same effective stress conditions. This is analogous to a field scenario considering progressively smaller tree roots at similar depths within a coarse-grained soil. To this end, three dimensional (3D) Discrete Element Method (DEM) simulations, capable of modelling particle-scale interactions, were employed to replicate the behaviour of rigid lateral root segments of different diameters interacting with a granular bed. The results were then compared with equivalent Finite Element Method (FEM) simulations, where the soil was modelled as a continuum and hence did not incorporate particle size effects, to identify any deviations from the continuum behaviour. Subsequently, the force–displacement behaviour observed from these simulations was incorporated within a numerical model of a flexible lateral root subject to rotation at one end (consistent with the loading seen during tree overturning), as these roots provide a large proportion of the anchorage resistance of a tree according to existing field (Coutts 1986; Crook and Ennos 1996) and laboratory physical testing (Zhang et al. 2023). A beam-on-non-linear-Winkler-foundation (BNWF) approach using $p$-$y$ curves from the FEM or DEM simulations was employed, to investigate the relative magnitude of particle size effects to other root-size dependent characteristics such as root stiffness and strength.

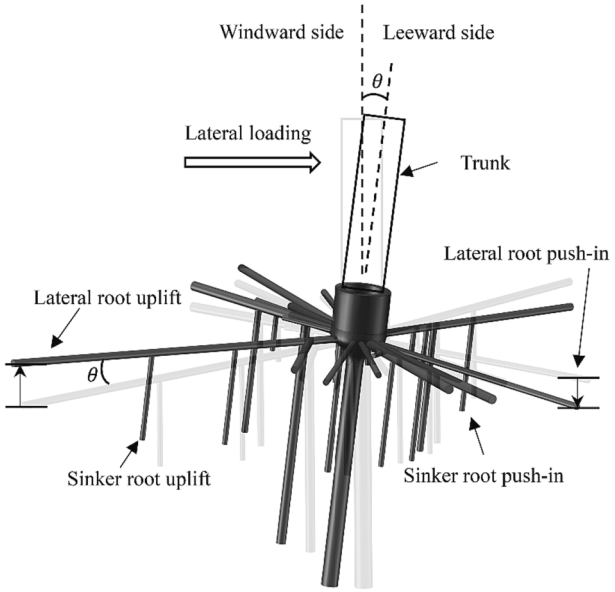


**Fig. 1.** A simplified root system under lateral loading.

## 2. Physical modelling of lateral root uplift for validation

### 2.1. Soil

A uniformly graded medium to fine sand (HST95 Congleton silica sand) was used for testing. This sand is a specific fraction of the sand extracted at Bent farm, Congleton, Cheshire, and has been widely used at the University of Dundee for physical model tests. The particle size distribution (PSD) of the sand is shown in Fig. 2, while some other index properties are summarised in Table 1. The coefficients of uniformity and curvature of the soil were 1.5 and 1, respectively, and its maximum and minimum density were 1.8 and 1.5 Mg/m$^3$, respectively. The critical state friction angle of the sand was 32$^\circ$ based on direct shear tests across a range of relative densities (9–93 %) and effective confining stresses (5–200 kPa), as reported by Al-Defae et al. (2013).

### 2.2. Physical testing of lateral root-soil interaction

The lateral root analogue investigated in this study was simplified to be straight, based on two field trees: a 27-year-old *Pinus pinaster* tree grown in a deep sandy spodosol in the "Landes de Gascogne" forest in south-west France (Danjon and Reubens 2008) and a 19-year-old *P. pinaster* tree grown in a shallower sandy spodosol in Cestas, France (Danjon et al. 2013), where in each case a large proportion of lateral roots were ~ 60 mm in diameter and located at ~ 130 mm below the soil surface. Correspondingly, a 60 mm diameter steel T-bar buried at 130 mm depth (denoted as $z_r$, from ground surface to the root centreline) was fabricated to simulate an idealised lateral straight cylindrical root segment at 1:1 (full) scale for validation of subsequent numerical models.

A test container with internal dimensions of 800 mm (length) × 500 mm (width) × 550 mm (height) was used. The length of the T-bar (i.e., the root analogue) was 430 mm (Fig. 3). The HST95 sand was initially air pluviated to create a uniform soil bed with a depth of 120 mm to the underside of the root with a relative density of 60–65 % (corresponding to the dry density 1.67 ± 0.01 Mg/m$^3$). The root analogue was then suspended above this soil and pluviation continued until the model root was buried to a depth of 130 mm (such that the cover depth $c = 100$ mm and $c/d_r = 1.67$). A water head 300 mm higher than the soil surface was applied at the bottom of the model soil for bottom-up saturation. To achieve drained behaviour, the model root was uplifted vertically at a rate of 0.0025 mm/s, which was one order of magnitude slower than the

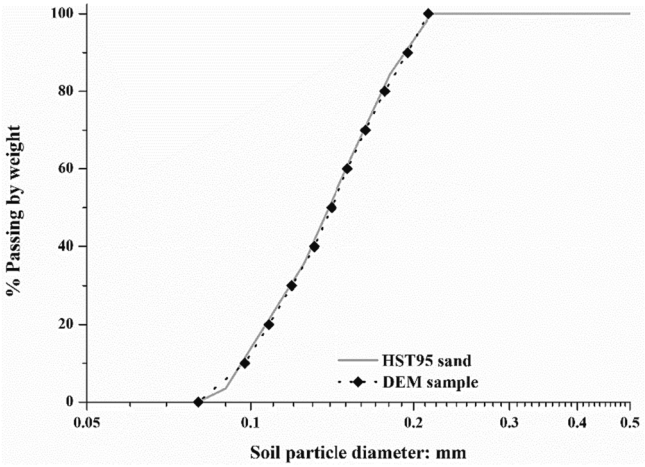


**Fig. 2.** Particle size distribution of experimental and numerical sands.

**Table 1**
HST95 sand key numerical parameters (after Al-Defae et al. 2013; Brown et al. 2019).

| Soil index properties | Value |
|---|---|
| Mean particle size ($D_{50}$): mm | 0.14 |
| Maximum particle size ($D_{100}$): mm | 0.21 |
| Minimum void ratio | 0.467 |
| Maximum void ratio | 0.769 |
| **DEM parameters** | **Value** |
| Specific gravity ($G_s$) | 2.65 |
| Shear modulus: GPa | 3 |
| Poisson's ratio | 0.3 |
| Particle friction coefficient | 0.264 |
| Interface friction coefficient (root) | 0.16 |
| **FEM parameters (corresponding to 60 % relative density)** | **Value** |
| Peak friction angle ($\phi'$): ° | 41 |
| Dilation angle ($\psi$): ° | 11 |
| Reference oedometer stiffness ($E_{oed}^{ref}$): MPa | 35.2 |
| Reference secant stiffness ($E_{50}^{ref}$): MPa | 44 |
| Reference unloading/reloading stiffness ($E_{ur}^{ref}$): MPa | 105.7 |
| Reference low strain shear modulus ($G_0^{ref}$): MPa | 118.8 |
| Reference shear strain ($\varepsilon_{s,0.7}$): % | 0.0169 |

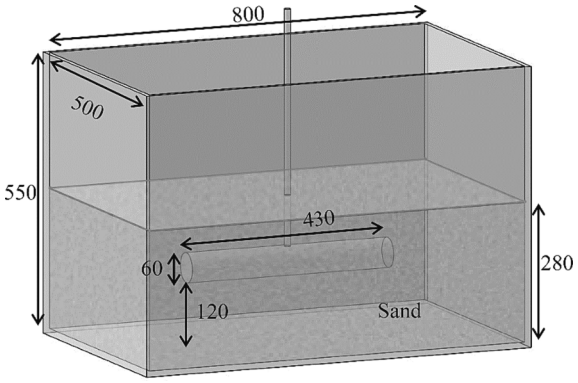


**Fig. 3.** Diagram of 1:1 physical test set-up for lateral root uplift test (all dimensions in mm).

drained loading rate adopted in previous direct shear tests of the same soil (i.e. 0.032 mm/s, Lauder, 2010), using a tension–compression loading frame (Instron 5985L7706, Instron Inc., US). The capacity of the load cell used to measure the uplift force was 30 kN with an accuracy of 1 mN. Force and displacement readings were logged at a sampling frequency of 1 Hz.

## 3. Numerical modelling and validation

### 3.1. Constitutive models and parameters

To model the root-soil interaction in DEM, Particle Flow Code (PFC) 3D 5.0.35 (Itasca Consulting Group, 2016) was employed. The mechanical interface interactions among particles and between the particle and root were modelled by a simplified Hertz-Mindlin contact model (Mindlin and Deresiewicz 1953). The contact model was calibrated to replicate the macroscopic mechanical behaviour of the HST95 sand. The particle size distribution (PSD) adopted was representative to the HST95 sand tested in the laboratory (see Fig. 2). The contact parameters (Table 1) for particle–particle interaction were calibrated against existing drained triaxial test data under a confining pressure of 60 kPa at two different relative densities (see Fig. 4; after Brown et al., 2019). Following Ciantia et al. (2016), the DEM implementation of the triaxial tests used representative element volumes (REVs), which, for the PSD of

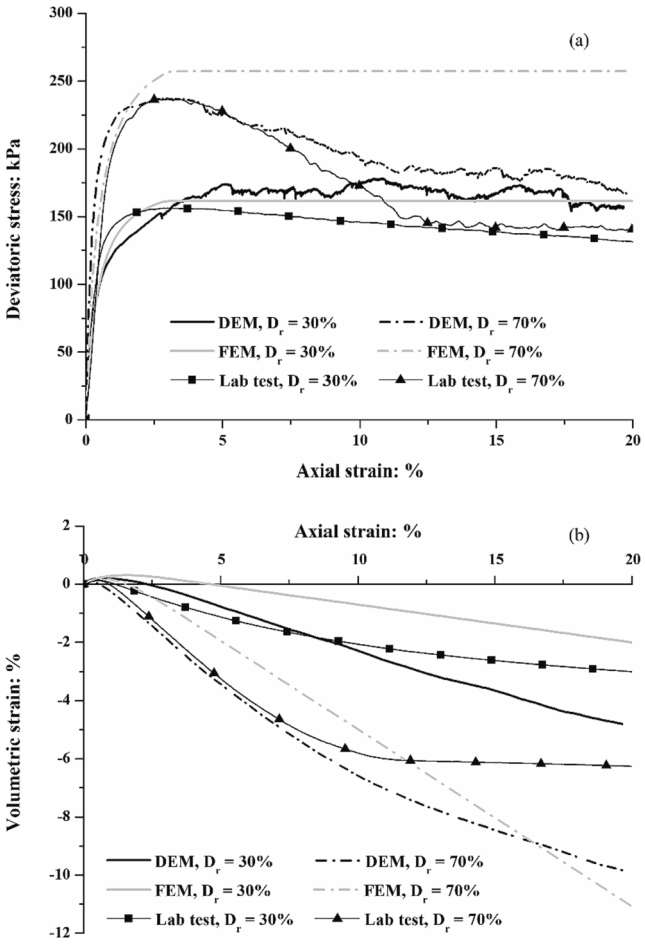


**Fig. 4.** Validation of triaxial tests of HST95 sand under a confining stress of 60 kPa: (a) Deviatoric stress - axial strain; (b) Volumetric strain - axial strain (DEM and laboratory data from Brown et al. 2019; FEM from this study).

the HST95 sand, consist of around 5000 particles (Brown et al. 2019). Sample generation used the radius expansion technique (Cundall and Strack 1979) followed by a consolidation phase to the required relative densities. Stress-controlled servo rigid frictionless walls were used to reach an effective confining pressure of 60 kPa. During shearing of the REV, the stress-controlled servo was maintained on the lateral boundaries at the desired confining (cell) pressure. The bottom boundary was fixed, while the top boundary was displaced in a strain-control manner. To attain a quasistatic response, wall strain rates were capped such the inertial number was always maintained less than.

$10^{-3}$ (Ciantia et al. 2018). Particle rotation was inhibited to simulate the interlocking effects of the sand, which was computationally efficient (Arroyo et al. 2011) and may be considered as a limit case for classical rolling-resistance contact models (Rorato et al. 2021). The coefficient of particle-structure interface friction was set to be 0.16 based on steel-soil direct shear interface tests.

To provide a continuum comparison, root-soil interaction was also simulated by two-dimensional (2D) plane-strain FEM simulations using PLAXIS 2019. A non-linear elasto-plastic constitutive model, called 'hardening soil with small strain stiffness' ('HS small'), was employed. The key soil parameters summarised in Table 1 were previously calibrated for the HST95 sand by Al-Defae et al. (2013) based on an extensive series of drained direct shear and oedometer compression tests.

Fig. 4 demonstrates the performance of both the DEM and FEM parameters under drained triaxial compression against element test data. When the axial strain was less than or equal to that resulting in peak

strength the shearing behaviour was generally well captured by both models. Beyond this point, however, the soil softening behaviour observed in the element tests can be reproduced by the DEM but not by the FEM when using the hardening soil model, as expected. The uplift/push-in resistance of individual lateral roots associated with peak strength (based on studies of uplift/push-in resistance of buried pipelines: (White et al. 2008; Wu et al. 2021) is of principal interest in this paper.

### 3.2. Modelling procedure

To reduce runtime, the dimension of the lateral root analogue and its burial depth were both scaled down by 20 times, the same scale factor as adopted in previous physical modelling studies of the same two root systems (Zhang et al. 2020). A 3D DEM model with periodic boundaries (Ciantia et al. 2018) in the out of plane dimension (root axis direction) was developed, at model scale, to recreate the approximate plane strain condition considered in the laboratory (Fig. 5(a)). To replicate the same effective stress conditions, an elevated acceleration field at 20 ***g*** should be imposed to a water-saturated model. However, to avoid having to explicitly simulate water in DEM, a lower ***g***-level at 12 ***g*** was applied to the dry model so that the effective stress regime was identical to that of saturated soil tested in the laboratory, following Eq. (1):

$$N_d = \left(1 - \frac{1}{G_s}\right) N_s \tag{1}$$

where $N_d$ and $N_s$ are ***g***-levels for dry and saturated case. The domain size in the DEM model (Table 2) was chosen to be large enough (i.e. $B_h/D_r = 6$, where $B_h$ is the width of the domain) to avoid unwanted boundary effects on the modelling of root-soil interaction. To efficiently generate a homogeneous and equilibrated DEM soil sample, the periodic cell replication method (PCRM) proposed by Ciantia et al. (2018) was employed. In PCRM, pre-equilibrated homogeneous $2.5D_{100}$-thick (0.53 mm) periodic cells at desired porosity, consistent with the laboratory test, were replicated to fill the entire domain. Further increasing the thickness of the chamber was observed to show negligible boundary effects on the root behaviour. The contact forces and interparticle reference gaps were then adjusted to achieve the desired initial gravitational stress state (Ciantia et al. 2018). The root analogue was represented by a rigid, wished-in-place cylinder which was displaced vertically upward, at a constant rate of 4 mm/s to limit the inertial number to be lower than $10^{-3}$ (Ciantia et al. 2019).

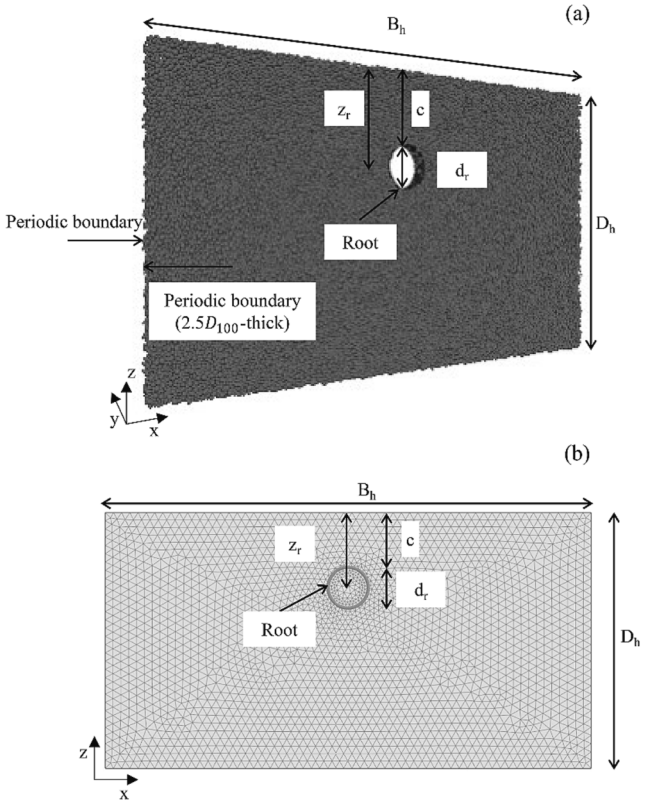


**Fig. 5.** Diagram of test set-up for numerical modelling of horizontal root in: (a) DEM; (b) FEM.

**Table 2**
Domains and root sizes of horizontal root simulations.

| $d_r/D_{50}$ | $N = N_s$ | $N_d$ | Uplift $D_h/d_r$ | Uplift $B_h/d_r$ | Push-in $D_h/d_r$ | Push-in $B_h/d_r$ | Notes |
|---|---|---|---|---|---|---|---|
| 28 | 15 | 9 | 4 | 6 | – | – | |
| 21 | 20 | 12 | 4 | 6 | 11 | 16 | $d_r$ = 3 mm, validation test |
| 17 | 25 | 15 | 5 | 8 | 13 | 20 | |
| 14 | 30 | 18 | 6 | 10 | 16 | 24 | |
| 11 | 38 | 23 | 7 | 12 | 20 | 29 | |
| 9 | 50 | 30 | 9 | 16 | 27 | 39 | |
| 6 | 75 | 45 | 14 | 24 | 40 | 59 | |
| 3 | 150 | 90 | 28 | 48 | – | – | |

To have a direct comparison with the DEM simulation, the 1:20 scaled model test was also simulated with a 2D plane strain FEM model (Fig. 5(b)), where a wished-in-place circular root was modelled with a rigid circular plate element. The FEM domain was discretised into 21,268 15-noded plane strain elements. Zero thickness interface elements were used to model root-soil interaction, thereby allowing for the opening of any gap at the root-soil interface in case of zero effective normal stress occurring during loading (no tension condition). The coefficient of lateral earth pressure $K_0$ was determined by Jaky's (Jaky 1944) formula (i.e. $K_0 = 1 - \sin\phi'$, where $\phi'$ is the soil peak friction angle). To model the process of uplift, a uniform vertical displacement was imposed to all of the nodes of the plate elements that formed the root analogue.

### 3.3. Validation of lateral root-soil interaction

Following the scaling laws shown in Table 3 (Nakahara et al. 2005), the force–displacement (*p-y*) curve obtained from the DEM simulation was scaled to the prototype scale for comparing with the physical model tests (Fig. 6). Note that the data directly obtained from the DEM was smoothed by applying the Adjacent-Averaging method to every 2500 data points. The overall shape of the curves from the laboratory test and the DEM (smoothed), especially post-peak softening behaviour at large displacement, were consistent with each other, although the DEM simulation slightly overestimated the peak uplift force by less than 10 % and displayed a higher pre-peak stiffness. The peak uplift force predicted by the FEM was also close, approximately 5 % lower than the model test. However, due to severe mesh distortion at large displacement, the FEM simulation could not proceed further than this, in contrast to the DEM that was able to simulate the complete uplift.

**Table 3**
Scale laws used in this study (after Nakahara et al. 2005).

| Parameter | Scaling law: Model/Prototype |
|---|---|
| Length/Depth | $1/N$ |
| Mass density | 1 |
| Acceleration | $N$ |
| Stiffness | 1 |
| Stress | 1 |
| Force | $1/N^2$ |
| Displacement | $1/N$ |

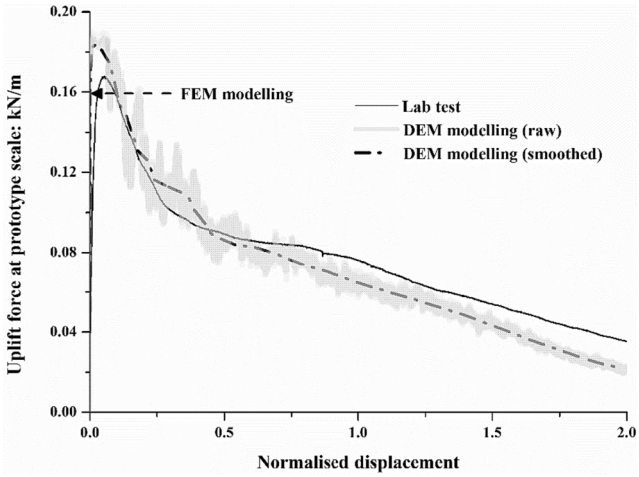


**Fig. 6.** Validation of lateral root uplift.

## 4. Parametric study of particle size effects

### 4.1. General description of modelling methodology

Particle size effects on lateral roots during both uplift and push-in movements were investigated using the validated DEM models. The principle of these simulations was to scale down the diameter ($d_r$) and buried depth ($z_r$) of a straight lateral root analogue by a variable factor $N$ and then to scale up the gravitational acceleration by $N$ times so that the prototype virtual model and stress regime were the same for all the simulations. However, the particle size was not scaled through this approach, so the number of soil particles in contact with the root would be proportionally reduced as $N$ increased. Thus, this modelling method is equivalent to selecting different scale factors to model the lateral root during the design of a centrifuge experiment. It is also a convenient way of changing only the ratio of $d_r/D_{50}$ while using identical DEM particle assemblies. Following the conventional scaling laws (e.g. Nakahara et al. 2005), force at prototype scale could be obtained by multiplying the simulated force in each case by $N^2$. The response obtained at prototype scale should be the same in all cases of different $N$, if particle size effects are absent. The prototype diameter and buried depth were selected to be 60 mm and 130 mm, respectively ($z_r/d_r = 2.2$), the same as that adopted in the validation experiment. The diameters of the scaled roots were informed by the sizes of individual roots considered in the 1:20 scale model tree root system ($d_r = 3$, 2.4, 2 and 1.6 mm) tested by Zhang et al. (2020). Additional smaller diameters (1.2 and 0.8 mm) were also considered to cover a wider range of $d_r/D_{50}$ (i.e. $< 10$; Table 2). For uplift cases only, $d_r = 4$ and 0.4 mm cases were added to further extend the range, based on the results from the initial simulations.

The rates of applied vertical uplift and push-in were set to be 4 mm/s for all cases to ensure that the loading process of the roots of different sizes remained quasi-static. The methods used to generate the DEM particle assembly in each case were the same as those used in the preceding validation section. The dimension of the domain in 4 mm case has the same $B_h/D_r$ and $D_h/D_r$ ratios with the 3 mm root case, and for other cases the $B_h$ and $D_h$ were determined to be the same as those adopted in the validation section. Corresponding FEM simulations were also conducted using the same dimensions as the DEM models for making direct comparison following the procedures used for model validation.

### 4.2. Uplift of lateral roots

Fig. 7(a) compares the uplift resistances at prototype scale obtained from DEM simulation of scaled lateral roots, which have the same prototype dimension. It is evident that as $d_r/D_{50}$ was reduced from 28 to 8,

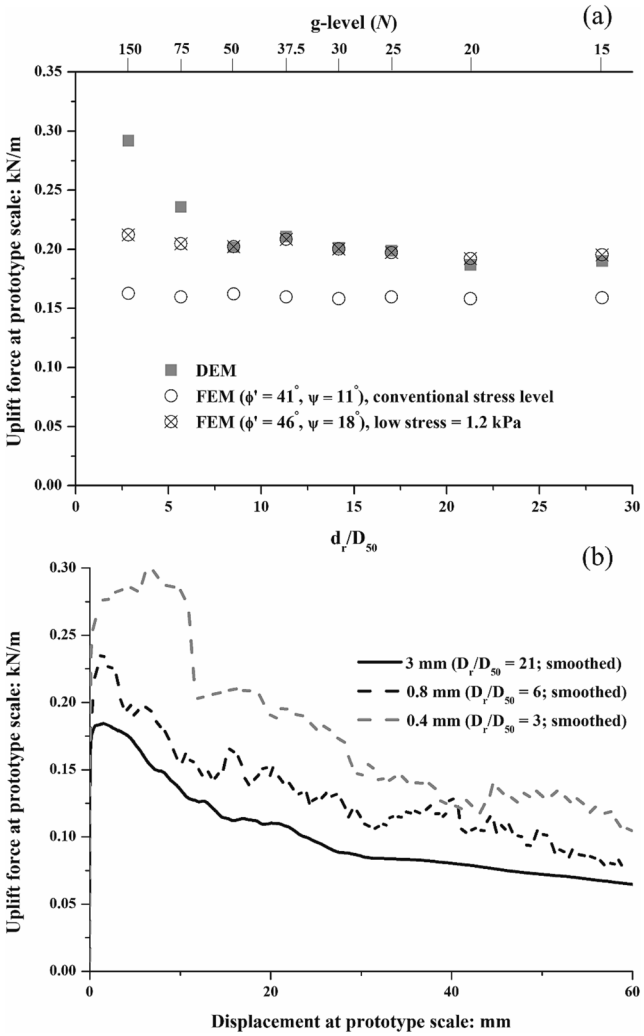


**Fig. 7.** (a) Uplift resistance of horizontal roots with different scale factors; (b) Load-displacement curves of 3, 0.8 and 0.4 mm roots from DEM uplift simulations.

the values of uplift resistance were similar; however, a substantial increase in the resistance was observed when $d_r/D_{50}$ was reduced below 8. The load–displacement curves of the 3, 0.8 and 0.4 mm roots (corresponding to $d_r/D_{50}$ of 21, 6 and 3, respectively) are depicted in Fig. 7(b), showing a noticeable increase in the uplift resistance when $d_r$ reduced to 0.8 mm. This suggests that $N = 50$ (which corresponds to $d_r/D_{50}$ of 8) is the maximum scale factor that would be free from particle size effects when testing a scaled 60 mm diameter tree root in HST95 sand on the centrifuge, or that the same root would begin to see particle size effects in the field in a gravelly soil with $D_{50} \geq 7.5$ mm. The threshold ratio of $d_r/D_{50}$ derived (i.e. 8) for this specific root-soil system was much smaller than those reported by Ovesen (1981) and Palmer et al. (2003), who found no obvious particle size effects on the uplift resistance of circular plates and pipelines down to threshold ratios of 44 and 80, respectively. This was because no further tests using increased scale factors were conducted in previous research due to the large prototype dimension of conventional geotechnical structures. However, the root analogue considered in the present study has a much smaller prototype dimension than other engineering structures such as plates and pipelines tested previously, such that lower structure-grain size ratios needed investigating.

For the FEM simulations, as expected, over the entire range of $d_r/D_{50}$, the prototype uplift resistance remained effectively constant because the soil in these simulations was considered to be a continuum where par-

ticle size effects were implicitly absent. Ignoring the particle size effect could lead to a substantial underprediction of the uplift resistance at large scale factors (e.g. ~ 40 % at $N = 150$). Even above the threshold $d_r/D_{50}$ value (i.e. 8), the resistance obtained from the FEM was approximately 15 % lower than that from the DEM. This discrepancy arises because the input peak strength and dilation angle used in FEM in Table 1 were those appropriate for conventional stress levels considered in routine laboratory testing for conventional geotechnical systems (friction and dilation angles of 41° and 11°, respectively) rather than the extremely low confining stress, 1.2 kPa, considered in the model tests. Bolton (1986) quantified the effects of dilation in terms of an increase in the soil peak friction angle as

$$\phi' - \phi'_{crit} = AI_R \tag{2}$$

where $A$ is a dimensionless factor to account for strain type ($A = 5$ for plane strain); $\phi'_{crit}$ is the soil friction angle at critical state (32° for the HST95 sand in this study); and $I_R$ is given by

$$I_R = I_D(Q - lnp') - R \tag{3}$$

where $I_D$ is the relative density of the sand, $p'$ is the mean effective confining stress of the soil; $Q$ and $R$ are fitting parameters according to the intrinsic sand characteristics, taken to be 10 and 1 respectively when $0 < I_R < 4$ (Bolton 1986). At low confining stress level, however, Chakraborty and Salgado (2010) suggested using $Q = 7.1 + 0.75lnp'$ (for plane strain) and $R = 1$, respectively. After obtaining a revised $\phi'$ using these expressions, following (Bolton 1986) the corresponding dilation angle $\psi$ can be calculated as

$$\phi' - \phi'_{crit} = 0.8\psi \tag{4}$$

Based on these calculations, the peak friction angle and the dilation angle at low confining stress were modified to be 46° and 18°, respectively. Using these values in the FEM simulations, the prediction of uplift resistance was much improved (Fig. 7), showing a consistent result with the DEM simulation for $d_r/D_{50}$ above the threshold value of 8.

### 4.3. Mechanisms controlling particle size effects during uplift

The DEM-computed velocity profile, at an uplift displacement of 0.02 $d_r$, where the uplift force peaked, is shown in Fig. 8 for two contrasting root diameters. It should be noted that particles with a velocity lower than 1/10th of the root velocity (i.e. 0.4 mm/s at model scale) are not presented as this is considered a threshold level between stationary and moving particles. White et al. (2008) and Giampa et al. (2017) used the assumption of a wedge of soil uplifted with shear planes inclined to the vertical at the dilation angle to develop analytical solutions based on limit equilibrium for the assessment of uplift capacity of pipelines and circular plate anchors, respectively. Under this assumption, the weight of the affected soil wedge ($W$) in plane strain can be calculated as

$$W = \gamma' z_r d_r + \gamma' z_r^2 tan\psi - \frac{\pi\gamma' d_r^2}{8} \tag{5}$$

where $\gamma'$ is the effective (buoyant) unit weight of the soil. White et al. (2008) assumed that the normal effective stress acting on the sliding planes was equal to the in-situ value inferred from $K_0$ conditions, in

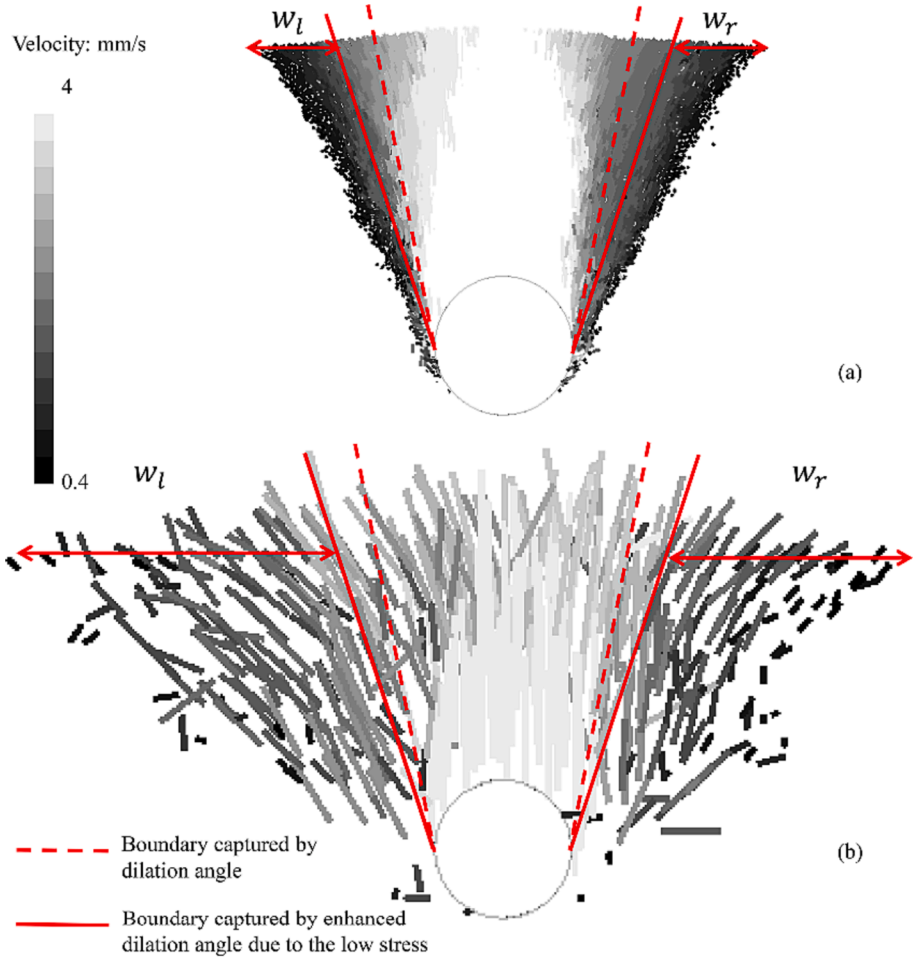


**Fig. 8.** Velocity field and particle tracks from DEM at 0.02 $d_r$ uplift displacement for: (a) 3 mm root; (b) 0.8 mm root.

which case the vertical force acting on the sliding block ($S$) can be calculated using:

$$S = \gamma' z_r^2 (\tan\phi' - \tan\psi)\left(\frac{1+K_0}{2} - \frac{(1-K_0)cos2\psi}{2}\right) \quad (6)$$

Giampa et al. (2017) reviewed previous studies and proposed a modified expression for $S$:

$$S = \gamma' z_r^2 (\tan\phi' - \tan\psi)cos(\phi' - \psi) \quad (7)$$

In this study, using Eq. (7) returns a higher value of $S$ than that by Eq. (6), such that a higher uplift resistance per unit length $P$ results, where:

$$P = W + S \quad (8)$$

As shown in Fig. 9, the results of the analytical solutions using White et al. (2008) and Giampa et al. (2017) were superimposed with the DEM simulation results given in Fig. 7. Note that both analytical solutions used the friction and dilation angles based on Eqs. (2) and (4) to capture the low confining stress effect. For $d_r/D_{50} > 8$, when particle size effects were negligible, the DEM simulations fell within the range suggested by the two analytical solutions. By plotting the dilation angles under conventional and low confining stress in the particle velocity profile (dashed and solid lines respectively in Fig. 8), it is apparent that considering enhanced dilation due to the low confining stress condition captured a larger volume of the affected soil block, however there were a significant number of particles outside the analytical soil block which appeared to also be mobilised in DEM, which could contribute some additional weight to the soil block. This was not accounted for by the analytical model and was expected to lead to an additional contribution to the horizontal root uplift capacity.

The width of this additional affected zone to the left and right of the analytical block ($w_l$ and $w_r$ in Fig. 8) were measured from DEM and the average values ($w$) normalised by mean particle size ($w/D_{50}$) in each case are presented in Fig. 10. A strong positive linear correlation can be obtained between $w/D_{50}$ and $d_r/D_{50}$ with $R^2 = 0.94$:

$$\frac{w}{D_{50}} = 0.56\frac{d_r}{D_{50}} + 3.2 \quad (9)$$

Considering the weight contribution from the additional affected zone (in terms of increasing the volume of the uplifted block) and incorporating this within the analytical model proposed by White et al. (2008), the uplift resistance per unit length $P$ can be modified as:

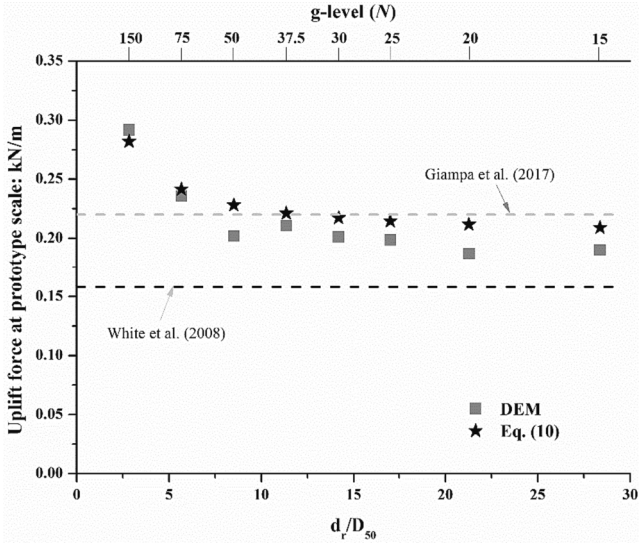


**Fig. 9.** Comparison of uplift force between DEM simulations and analytical studies.

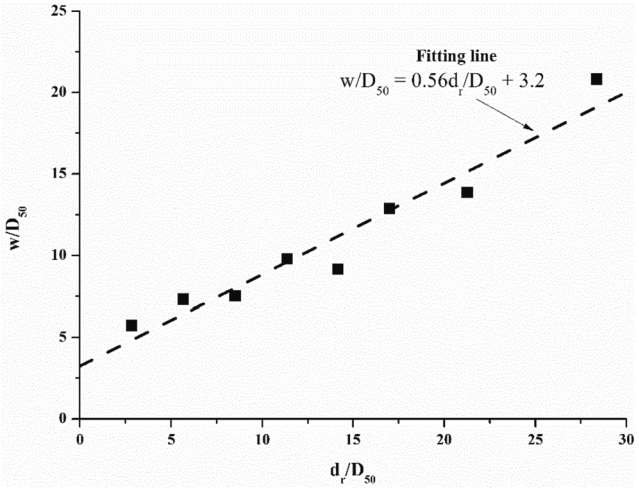


**Fig. 10.** Relationship between the width of additional affected zone and root diameter.

$$P = \gamma' z_r d_r + \gamma' z_r^2 tan\psi + \gamma'(0.56d_r + 3.2D_{50})z_r + \gamma' z_r^2(\tan\phi'_{max} - \tan\psi)\left(\frac{1+K_0}{2} - \frac{(1-K_0)cos2\psi}{2}\right) - \frac{\pi\gamma' d_r^2}{8} \quad (10)$$

This modified expression resulted in a much better match with the DEM simulations (Fig. 9), capturing the particle size effect as $d_r/D_{50}$ reduces and the widened zone of shearing becomes proportionally larger compared to the diameter of the root. Indeed, as shown in Fig. 8, the dimension of the additional affected zone relative to the 0.8 mm root (i.e. $w/d_r$; Fig. 8b) was larger than that compared to the 3 mm root (Fig. 8a) due to the intercept of 3.2 in Eq. (9). This term is not associated with root diameter and results in particle size effects (through $3.2D_{50}$ in Eq. (10)) for fine lateral roots (or large roots at highly reduced scale) but becomes negligible for coarse roots (or lower scale factors). However, the magnitude of this term may be dependent on soil particle shape, relative density, particle size distribution, and friction angle. How this term might be correlated with such soil properties requires further systematic simulations in the future.

### 4.4. Behaviour during push-in

The peak push-in force with first 10 mm penetration is compared at prototype scale in Fig. 11(a), with the force–displacement curve of the roots of maximum and minimum simulated diameter shown in Fig. 11 (b). Although some differences were observed in terms of the stiffness of the push-in curve, possibly due to the lower $B_h/d_r$ ratio for bigger roots, the prototype values of push-in resistance of the model roots of different diameters at model scale in the DEM simulation were largely similar, within the range of $d_r/D_{50}$ examined. This means that particle size effects were not prominent under this loading condition. Other studies have investigated particle size effects for other shallow penetration problems, such as Toyosawa et al. (2013). They explored the case of shallow foundations (of diameter $d_r$) at the ground surface and those at an embedment depth $z_r$ of 0.5 $d_r$, finding a reduction in the minimum $d_r/D_{50}$ ratio to avoid particle size effects as $z_r/d_r$ increased (from $d_r/D_{50} = 50$ at $z_r/d_r = 0$ to $d_r/D_{50} = 33$ at $z_r/d_r = 0.5$). This suggests that particle size effects may vanish as structures are more deeply buried, i.e. $z_r/d_r$ gets larger (Fig. 12). In this paper, the root analogues were buried at $z_r/d_r = 2.2$ and no particle size effects were identified during vertical penetration (at least down to $d_r/D_{50} = 6$), consistent with the findings reported by Toyosawa et al. (2013). As in the uplift case, when ignoring the effects of the low confining stress regime on the continuum strength parameters, the results obtained from the FEM simulations were consistently lower than those from the DEM (~45 % for the push-in

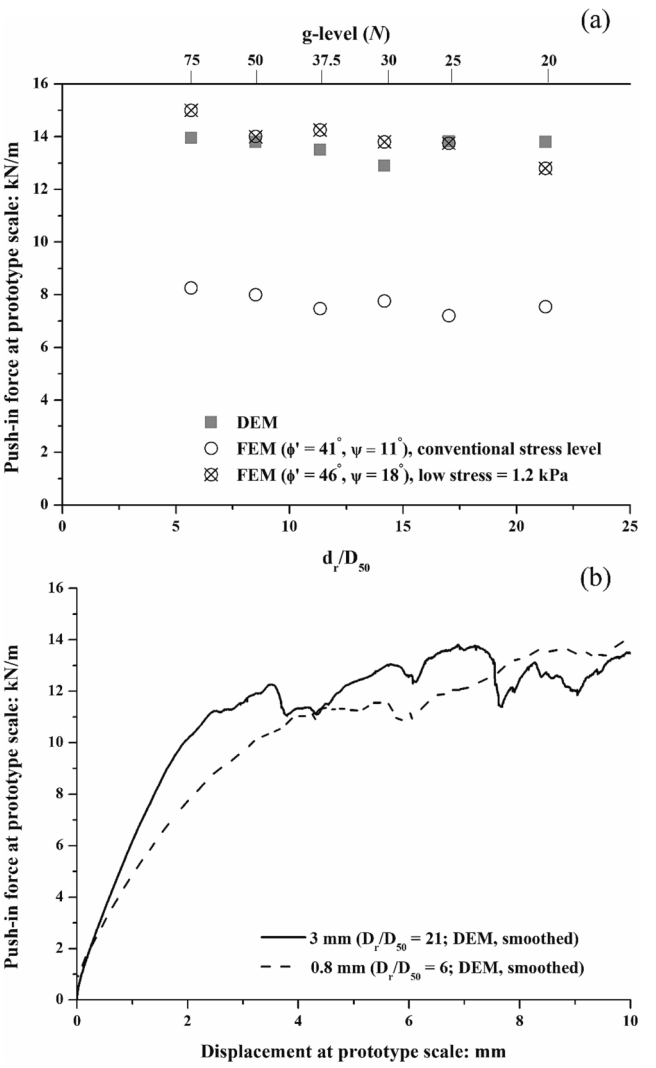


**Fig. 11.** (a) Push-in resistance of horizontal roots with different scale factors; (b) Load-displacement curves of 3 and 0.8 mm roots from DEM push-in simulations.

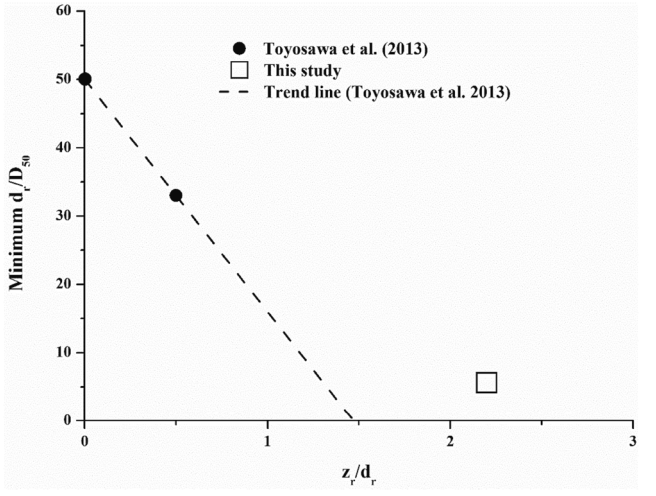


**Fig. 12.** Minimum diameter of rigid objects to avoid particle size effects at different burial depths.

condition). As before, adjusting the strength parameters to account for the low-stress effects (i.e. using Eqs. (2) and (4)) substantially improved the prediction accuracy of the FEM (Fig. 11(a)).

## 5. Modelling of whole lateral root behaviour under tree overturning

### 5.1. Numerical simulation set-up and procedures

In addition to the root size effects on soil-structure interaction properties explored in the previous sections, roots themselves typically exhibit material properties which are dependent on diameter (Schwarz et al. 2010; Mao et al. 2012):

$$T_r = \alpha_T d_r^{\beta_T} \tag{11}$$

$$E_r = \alpha_E d_r^{\beta_E} \tag{12}$$

where $T_r$ is the tensile strength, $E_r$ is the root Young's modulus and $\alpha_T$, $\beta_T$, $\alpha_E$, and $\beta_E$ are empirical fitting parameters. To explore the relative magnitude of these root size dependencies, numerical simulations were conducted, adopting a BNWF approach to model a long flexible lateral root subject to rotation at one end to simulate the action applied by the trunk during tree overturning, with the force–displacement behaviour obtained from previous DEM/FEM simulations incorporated.

The BNWF approach, which has significant advantages in computational efficiency compared to continuum FE models of root-soil interaction (e.g. Mickovski et al., 2011; Dupuy et al., 2007), was conducted using the non-linear FE programme ABAQUS to solve the beam-on-spring problem. As shown in Fig. 1, the windward lateral roots rotate about the centreline of the root system upon an external loading. A schematic diagram of this problem, as discretised within the BNWF framework, is depicted in Fig. 13. The root was modelled using deformable 2D beam elements, which are flexible in both shear and bending. A linear elastic-perfectly plastic model was used to model the stress–strain behaviour of the root. A series of fixed rigid vertical beams, which sat at a close and uniform vertical offset (i.e. 0.0004 mm) from the discrete nodes along the root, were established to prescribe a fixed boundary condition. Non-linear *p-y* springs were then connected between the root and the fixed beams to capture the root-soil interaction, with this behaviour being parametrised from the DEM/FEM simulations reported earlier. Compared with the traditional *p-y* method for small deformations (e.g. lateral loading of piles), where the springs are considered to remain perpendicular to the original position of the root before loading, in the present study the force always acted perpendicular to the displaced root section, such that the analyses would be representative at large applied rotations (see Meijer et al. 2019). This was achieved by using a connector element with the Cartesian type and a rotating local reference frame in ABAQUS.

An example of spring properties for a 3 mm root is shown in Fig. 14 (a). Since no scale effects related to particle size were observed when the root was pushed into the soil, the curve up to the peak force obtained from FEM was used, with the plateau added post-peak. The uplift properties of the spring is detailed in Fig. 14(b). In the case of DEM being used to define *p-y* curves, DEM simulation data was used directly as the

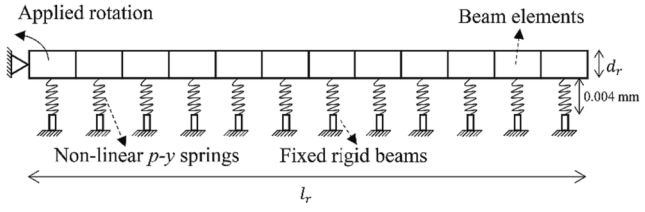


**Fig. 13.** Schematic diagram (not to scale) of root-soil system undergoing rotation loading (BNWF model).

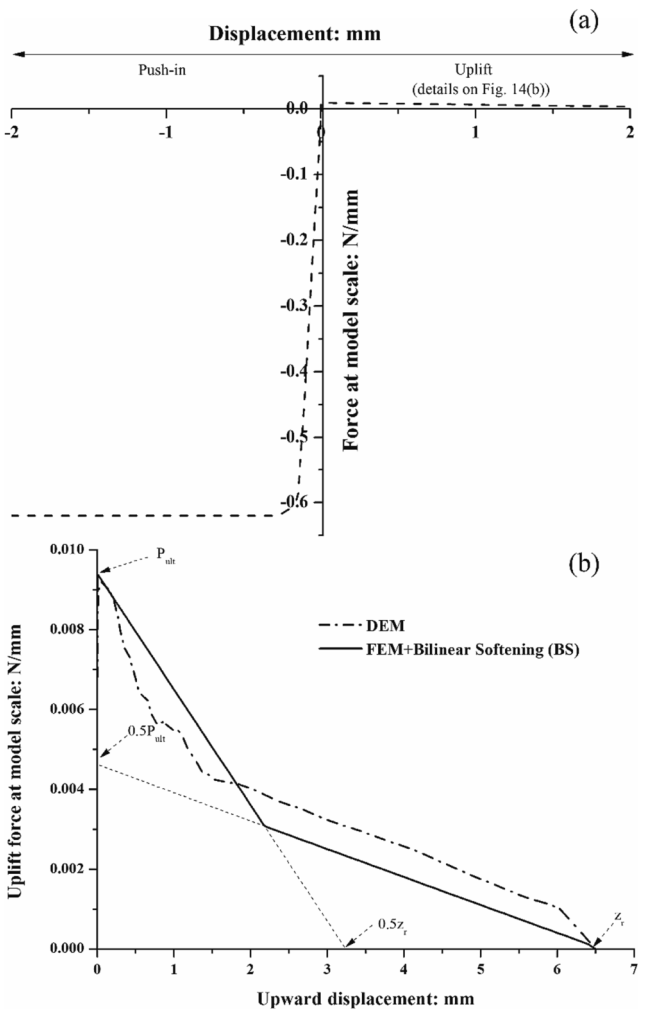


**Fig. 14.** (a) An example of the *p*–*y* curve for 3 mm lateral root; (b) Specification of uplift properties.

complete uplift process was simulated. Due to difficulties in simulating large (post-peak) deformation in FEM, for FEM defined uplift *p*-*y* curves, bilinear softening (BS; Fig. 14(b)) was assumed beyond the displacement $\delta_{ult}$ corresponding to the peak force ($p_{ult}$) from FEM, to complete the response over the complete extraction of a segment from the ground. The inflection point was determined as the intersection of the line connecting (0, $\frac{P_{ult}}{2}$) and ($z_r$, 0) and the line connecting ($\delta_{ult}$, $P_{ult}$) and ($\frac{z_r}{2}$, 0). The end point was ($z_r$, 0) to represent the uplift force becoming zero when the root leaves the soil. A hinged connection with fixed conditions in the horizontal and vertical directions was incorporated at the loading point to prevent any unwanted movement during rotation (applied through displacement control). Other than at this point, movement of the root was unrestrained, other than by the spring reactions.

The simulations of lateral root uplift (anticlockwise rotation in Fig. 13) conducted and the corresponding input parameters are summarised in Table 4. Initially, a 3 mm diameter root was simulated. The root was 150 mm long (simulations LR04 and LR05) according to the 1:20 scale model of a 60 mm diameter root from centrifuge model testing reported by Zhang et al. (2020). The scaled roots, made of 3D printed (layered) Acrylonitrile Butadiene Styrene (ABS) plastic in this study, were found to display diameter dependency in both tensile strength and Young's modulus similar to plant roots i.e. following negative power laws. According to a series of bending tests on root analogues of varying diameter conducted by Liang et al. (2015), the fitting parameters for Eqs. (11) and (12), $\alpha_T$, $\beta_T$, $\alpha_E$, $\beta_E$, were 164.7, −0.52, 7.27 and −0.79, respectively, where $T_r$, $E_r$, $d_r$ are in MPa, GPa, and mm, respectively and the Poisson ratio of ABS plastic was taken as 0.35.

The number of springs, controlling the size of the discretised elements along the root, was determined based on a sensitivity analysis. It was reduced from 1 spring/mm until a noticeable difference appeared on the computed moment-rotation curves. An example of results for 3 mm diameter root (length of 150 mm; LR04) is shown in Fig. 15. It can be seen that when the spring density was reduced to 0.5/mm (i.e. 75 springs over 150 mm root length), the root behaviour was almost identical to the initial condition (1)/mm). However, when the spring density was 0.033/mm, the moment capacity was overestimated by approximately 20 %. Note that 0.2/mm (corresponding to 30 springs) can be considered as the threshold value since the efficiency could be improved by 2.5 times with limited discrepancies observed, compared with the finest case of 1/mm.

A subsequent set of simulations were conducted considering the same prototype but simulated at different scale factors, with only the *p*-*y* parameters changed (i.e. only $d_r/D_{50}$ changed with constant root properties; LR08 and LR09) and with both the *p*-*y* and material properties being a function of $d_r$ (LR10 and LR11) to investigate the relative magnitude of root-size effects associated with $d_r/D_{50}$ and with $E_r$ and $T_r$

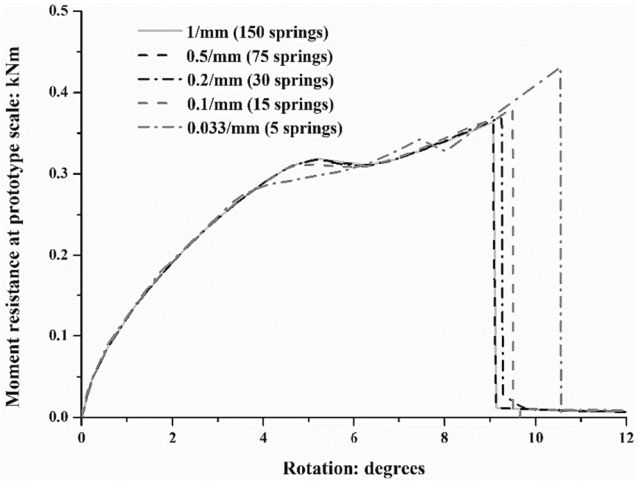


**Fig. 15.** Results of sensitivity analysis to determine an optimised number of springs to model the behaviour of a lateral root with 3 mm diameter.

**Table 4**
Simulations of whole lateral root uplift.

| Simulation ID | *N* | Diameter ($d_r$): mm | $d_r/D_{50}$ | Length ($l_r$): mm | Young's modulus ($E_r$): GPa | Tensile strength ($T_r$): MPa | *p*-*y* property |
|---|---|---|---|---|---|---|---|
| LR04 | 20 | 3.0 | 21 | 150 | 3.04 | 93.0 | FEM + BS |
| LR05 | 20 | 3.0 | 21 | 150 | 3.04 | 93.0 | DEM |
| LR08 | 75 | 0.8 | 6 | 40 | 3.04 | 93.0 | FEM + BS |
| LR09 | 75 | 0.8 | 6 | 40 | 3.04 | 93.0 | DEM |
| LR10 | 75 | 0.8 | 6 | 40 | 8.68 | 185.0 | FEM + BS |
| LR11 | 75 | 0.8 | 6 | 40 | 8.68 | 185.0 | DEM |

when scaling field cases in physical model tests. LR08 and LR10 were also separately rotated clockwise (Fig. 13) to study scale effects related to material properties when the whole root was pushed into the soil.

### 5.2. Scale effects on whole lateral root rotational behaviour

Fig. 16 compares the moment-rotation curves, expressed at prototype scale, obtained from the simulations LR04, LR05, LR08 and LR09, where lateral roots had the same prototype and could be considered as a geometrically scaled model choosing different scale factors $N$. The $E_r$ and $T_r$ of the root used in all these simulations were identical, and they were determined based on the 3 mm ABS plastic rod. In this case, the moment resistances should be the same if particle size effects in the root-soil interaction are absent. The curves are in excellent agreement during the first 2.5° rotation, and the initial rotational stiffness were practically the same. Beyond this, some discrepancies appeared. For the cases using $p$-$y$ properties derived from FEM + BS (i.e. LR04 and LR08) their moment capacities (at approximately 9° rotation) are similar, around 0.37 kNm. The 5 % difference was due to differences in meshing between FEM simulations for the different diameter cases. The moment resistance of the 0.8 mm root, using the $p$-$y$ property derived from the DEM simulation, was approximately 20 % higher, compared with that of the 3 mm root due to the difference in $d_r/D_{50}$ (i.e. LR09 and LR05), implying particle size effects, similar to those illustrated in Fig. 7. Sharp drops of moment were observed at the end of simulations because roots were pulled out of the soil, where the force from most springs became to 0 under the large relative displacement. Moreover, it can be seen that the uplift resistances of the 3 mm root, in which the particle size effect could be neglected, using the properties derived from either DEM or FEM + BS (LR05 and LR04) are rather close, suggesting the suitability of the BS assumption for approximation of post-peak behaviour (in the absence of particle size effects) such that simple plane strain FEM simulations may be used to parameterise $p$-$y$ curves in cases of sufficiently high $d_r/D_{50}$, rather than computationally expensive DEM simulations.

The simulations LR10 and LR11 had the same condition as LR08 and LR09, respectively, except that $T_r$ and $E_r$ were varied according to Eqs. (11) and (12) to consider the effects of diameter-dependency, which existed in physical model tests. Comparisons of the moment-rotation curves of these four simulations are depicted in Fig. 17(a). The results show that increasing the $E_r$ (from 3 to 8.7 GPa) increased both the initial stiffness and the moment resistance by approximately 2.5 and 1.5 times. However, this in turn made the root response more brittle, having a much lower rotation angle corresponding to the peak resistance ($\theta_p$), by approximately 50 %. Note that no plastic failure appeared within the root in any of the simulations, indicating that the soil had been

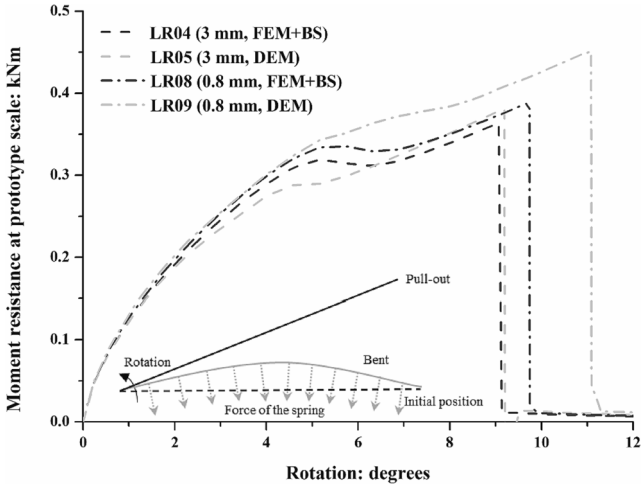


**Fig. 16.** Scale effects related to particle on root moment-rotation curve.

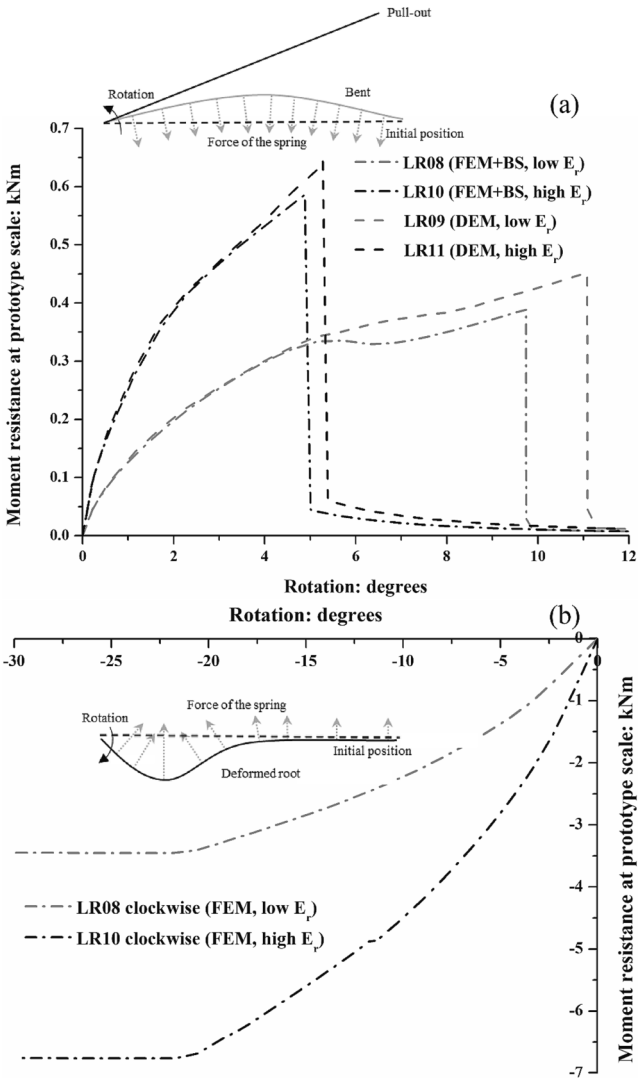


**Fig. 17.** Scale effects related to Young's modulus on root moment-rotation curve: (a) anticlockwise rotation; (b) clockwise rotation.

mobilised to its peak resistance before the roots broke and that the differences in root behaviour shown in Fig. 17(a) were due to the variation of the root Young's modulus rather than the tensile strength. Fig. 17(b) compares the cases of LR08 and LR10 but with the loading in the clockwise direction to simulate the whole lateral root pushed into the soil. In contrast to uplift cases, roots started yielding at 10° rotation and fully yielded at 21° rotation. In this case, the tensile strength of the root controlled the moment capacity, which was defined by the roots yielding and increased by approximately a factor of two resulting from the increase of $T_r$ from 93 to 185 MPa. The stiffness of the root contribution to overturning resistance is also increased with increasing $E_r$, as with the uplift cases in Fig. 17(a). While it is common to measure tensile strength of plant roots, Young's modulus is rarely reported in the literature. The results here demonstrate the importance of the parameter on the contributions of individual lateral roots to tree overturning stability.

## 6. Conclusions

This study has presented an investigation into potential root size effects that may arise in the transverse uplift or push-in of horizontally-orientated plant roots, such as the lateral roots of trees during overturning. 3D DEM numerical simulations were validated against laboratory uplift tests and were then employed to work as a 'virtual centrifuge'

to replicate the behaviour of lateral root segments of different diameters interacting with a granular bed and allow the ratio of root to particle diameter to be changed with the same prototype geometry and confining stress conditions. Results were compared with validated FEM simulations, where the soil was considered as a continuum and strength parameters representative for low confining stresses were used.

It was found that a change in $d_r/D_{50}$ did not significantly affect the push-in resistance. This implies that estimates of this element of resistance could be based on conventional continuum analytical approaches (e.g. bearing capacity of buried pipelines). In terms of the uplift resistance, particle size effects were observed when $d_r/D_{50}$ was lower than 8, arising from the dimension of the additional uplifted soil block above the root with a width of $3.2D_{50}$, which is significant for a fine root but negligible for a coarse root. This was incorporated into an analytical expression for uplift resistance which validated well against the DEM data.

A series of simulations of whole lateral root rotation (consistent with tree overturning) were then performed in which a BNWF approach using *p-y* curves were obtained based on the previous DEM or FEM results. Due to difficulties in simulating large deformation in FEM, a simplified Bilinear Softening (BS) approximation was assumed to complete the uplift curve of the root post-peak. The scale effects related to particle size affected the peak moment resistance in uplift at prototype scale by approximately 20 % when $d_r/D_{50}$ was reduced from 21 to 6 (corresponding to simulation of a 60 mm diameter root at either $N = 20$ or 75, respectively) and when root material properties were held constant. Comparatively, the variation in material properties with diameter typical of plant roots (i.e. following a negative power law) had a much larger controlling effect on the root moment capacity and stiffness when the whole root was uplifted and when pushed into the soil. In addition, $E_r$ was important in the uplift case, where stiffer and stronger roots resulted in a reduction of $\theta_p$ (rotation at failure) and made the root response more brittle, while the moment capacity was principally controlled by $T_r$ in the push-in case.

The results can be used to inform the design of physical model (e.g. centrifuge) tests of root-soil systems in terms of the selection of appropriate scale factors, and also provide guidance on input parameters for root-soil interaction models at field (1:1) scale. Further research using different particle size distributions, and thus varying $d_r/D_{50}$ through different values of $D_{50}$, along with corresponding physical tests, are required to generalise these findings.

## Declaration of Competing Interest

The authors declare that they have no known competing financial interests or personal relationships that could have appeared to influence the work reported in this paper.

## Data availability

Data will be made available on request.

## Acknowledgements

The first author would like to acknowledge the financial support of the China Scholarship Council (CSC) and the Norman Fraser Design Trust. The fourth author would like to acknowledge the funding provided by the Research Grants Council of the Hong Kong Special Administrative Region, (CRF/C6006-20G and 16202422) and the National Natural Science Foundation of China (NSFC) under the Excellent Youth Scientist Scheme (H. K. & Macau) (project no. 51922112). The sixth author would like to acknowledge the funding provided by The National Natural Science Foundation of China (NSFC) (Nos: 52008368, 52378373).

## References

Al-Defae, A.h., Caucis, K., Knappett, J.a., 2013. Aftershocks and the whole-life seismic performance of granular slopes. Géotechnique. 63, 1230–1244. https://doi.org/10.1680/geot.12.P.149.

Arroyo, M., Butlanska, J., Gens, A., et al., 2011. Cone penetration tests in a virtual calibration chamber. Géotechnique 61, 525–531. https://doi.org/10.1680/geot.9.P.067.

Athani, S., Kharel, P., Airey, D., Rognon, P., 2017. Grain-size effect on uplift capacity of plate anchors in coarse granular soils. Géotechnique Lett 7, 167–173.

Bałachowski, L., 2007. Size effect in centrifuge cone penetration tests. Arch Hydroengineering Environ Mech 54, 161–181.

Bolton, M.D., 1986. The strength and dilatancy of sands. Géotechnique 36, 65–78. https://doi.org/10.1680/geot.1986.36.1.65.

Brown, M., Sharif, Y., Ciantia, M., Knappett, J., Davidson, C., Cerfontaine, B., Robinson, S., 2019. Numerically modelling the installation and loading of screw piles using DEM. In: 1st International Symposium on Screw Piles for Energy Applications.

Chakraborty, T., Salgado, R., 2010. Dilatancy and shear strength of sand at low confining pressures. Jasce Ournal Geotech Geoenvironmental Eng 136, 527–532. https://doi.org/10.1061/(ASCE)GT.1943-5606.0000237.

Ciantia, M., Arroyo, M., Calvetti, F., Gens, A., 2016. Directional response of a reconstituted fine-grained soil - Part II : Performance of different constitutive models. Int. J. Numer. Anal. Meth. Geomech. 40, 1773–1798. https://doi.org/10.1002/nag.

Ciantia, M.O., Boschi, K., Shire, T., Emam, S., 2018. Numerical techniques for fast generation of large discrete-element models. Proc Inst Civ Eng - Eng Comput Mech 171, 147–161. https://doi.org/10.1680/jencm.18.00025.

Ciantia, M., O'Sullivan, C., Jardine, R.J., 2019. Pile penetration in crushable soils: Insights from micromechanical modelling. In: 17th European Conference on soil Mechanics and Geotechnical Engineering (ECSMGE 2019). International Society for Soil Mechanics and Geotechnical Engineering. https://doi.org/10.32075/17ECSMGE-2019-1111.

Coutts, M.P., 1986. Components of tree stability in sitka spruce on peaty gley soil. Forestry 59, 173–197. https://doi.org/10.1093/forestry/59.2.173.

Crook, M.J., Ennos, A.R., 1996. The anchorage mechanics of deep rooted larch, Larix europea × L. japonica. J. Exp. Bot. 47, 1509–1517. https://doi.org/10.1093/jxb/47.10.1509.

Cui, P., Lin, Y.M., Chen, C., 2012. Destruction of vegetation due to geo-hazards and its environmental impacts in the Wenchuan earthquake areas. Ecol. Eng. 44, 61–69. https://doi.org/10.1016/j.ecoleng.2012.03.012.

Cundall, P.A., Strack, O.D.L., 1979. A discrete numerical model for granular assemblies. Géotechnique 29, 47–65.

Danjon, F., Caplan, J.S., Fortin, M., Meredieu, C., 2013. Descendant root volume varies as a function of root type: estimation of root biomass lost during uprooting in Pinus pinaster. Front. Plant Sci. 4, 1–16. https://doi.org/10.3389/fpls.2013.00402.

Danjon, F., Reubens, B., 2008. Assessing and analyzing 3D architecture of woody root systems, a review of methods and applications in tree and soil stability, resource acquisition and allocation. Plant and Soil 303, 1–34. https://doi.org/10.1007/s11104-007-9470-7.

Dupuy, L.X., Fourcaud, T., Lac, P., Stokes, A., 2007. A generic 3D finite element model of tree anchorage integrating soil mechanics and real root system architecture. Am. J. Bot. 94, 1506–1514. https://doi.org/10.3732/ajb.94.9.1506.

Garnier, J., Gaudin, C., Springman, S.M., et al., 2007. Catalogue of scaling laws and similitude questions in geotechnical centrifuge modelling. Int J Phys Model Geotech 7, 01–23. https://doi.org/10.1680/ijpmg.2007.070301.

Giampa, J.R., Bradshaw, A.S., Schneider, J.A., 2017. Influence of dilation angle on drained shallow circular anchor uplift capacity. Int. J. Geomech. 17, 04016056. https://doi.org/10.1061/(asce)gm.1943-5622.0000725.

Harnas, F.R., Rahardjo, H., Leong, E.C., et al., 2016. Stability of containerized urban street trees. Landsc. Ecol. Eng. 12, 13–24. https://doi.org/10.1007/s11355-015-0272-4.

Jakob, M., Lambert, S., 2009. Climate change effects on landslides along the southwest coast of British Columbia. Geomorphology 107, 275–284. https://doi.org/10.1016/j.geomorph.2008.12.009.

Jaky, J., 1944. The coefficient of earth pressure at rest. J Soc Hungarian Archit Eng 78, 355–358.

Karimzadeh, A.A., Leung, A.K., Hosseinpour, S., et al., 2021. Monotonic and cyclic behaviour of root-reinforced sand. Can. Geotech. J. 58, 1915–1927. https://doi.org/10.1139/cgj-2020-0626.

Karimzadeh, A.A., Leung, A.K., Gao, Z., 2022. Shear strength anisotropy of rooted soils. Geotechnique. https://doi.org/10.1680/jgeot.22.00103.

Lauder K (2010) The performance of pipeline ploughs. 210.

Lehane, B.M., Gaudin, C., Schneider, J.A., 2005. Scale effects on tension capacity for rough piles buried in dense sand. Géotechnique 55, 709–719. https://doi.org/10.1680/geot.2005.55.10.709.

Lehane, B.M., White, D.J., 2005. Lateral stress changes and shaft friction for model displacement piles in sand. Can. Geotech. J. 42, 1039–1052. https://doi.org/10.1139/t05-023.

Liang, T., Knappett, J.A., 2017. Centrifuge modelling of the influence of slope height on the seismic performance of rooted slopes. Géotechnique 67, 855–869. https://doi.org/10.1680/jgeot.16.P.072.

Liang, T., Knappett, J.A., Duckett, N., 2015. Modelling the seismic performance of rooted slopes from individual root–soil interaction to global slope behaviour. Géotechnique 65, 995–1009. https://doi.org/10.1680/jgeot.14.P.207.

Mao, Z., Saint-André, L., Genet, M., et al., 2012. Engineering ecological protection against landslides in diverse mountain forests: Choosing cohesion models. Ecol. Eng. 45, 55–69. https://doi.org/10.1016/j.ecoleng.2011.03.026.

McCarthy, J.K., Hood, I.A., Brockerhoff, E.G., et al., 2010. Predicting sapstain and degrade in fallen trees following storm damage in a Pinus radiata forest. For. Ecol. Manage. 260, 1456–1466. https://doi.org/10.1016/j.foreco.2010.07.044.

Meijer, G.J., Wood, D.M., Knappett, J.A., Bengough, G.A., 2019. Analysis of coupled axial and lateral deformation of roots in soil. Int. J. Numer. Anal. Meth. Geomech. 43, 684–707. https://doi.org/10.1002/nag.2880.

Mickovski, S.B., Bransby, M.F., Bengough, A.G., et al., 2010. Resistance of simple plant root systems to uplift loads. Can. Geotech. J. 47, 78–95. https://doi.org/10.1139/T09-076.

Mickovski, S.B., Stokes, A., van Beek, R., et al., 2011. Simulation of direct shear tests on rooted and non-rooted soil using finite element analysis. Ecol. Eng. 37, 1523–1532. https://doi.org/10.1016/j.ecoleng.2011.06.001.

Mindlin, R., Deresiewicz, H., 1953. Elastic spheres in contact under varying oblique forces. J Appl Meechanics ASME 20, 327–344. https://doi.org/10.1007/978-1-4613-8865-4_35.

Nakahara, T., Iai, S., Tobita, T., 2005. Generalised scaling relations for dynamic centrifuge tests. Géotechnique 55, 355–362. https://doi.org/10.1680/geot.2005.55.5.355.

Ovesen, N.K., 1981. Centrifuge tests of the uplift capacity of anchors. In: 10th International Conference of Soil Mechancis and Foundation Engineering, pp. 717–722.

Palmer, A.C., White, D.J., Baumgard, A.J., et al., 2003. Uplift resistance of buried submarine pipelines: Comparison between centrifuge modelling and full-scale tests. Géotechnique 55, 338–340. https://doi.org/10.1680/geot.55.4.338.65484.

Rorato, R., Arroyo, M., Gens, A., et al., 2021. Image-based calibration of rolling resistance in discrete element models of sand. Comput. Geotech. 131 https://doi.org/10.1016/j.compgeo.2020.103929.

Schwarz, M., Lehmann, P., Or, D., 2010. Quantifying lateral root reinforcement in steep slopes - from a bundle of roots to tree stands. Earth Surf Process Landforms 35, 354–367. https://doi.org/10.1002/esp.1927.

Sinnreich, J., 2011. The scaling effect of bored pile radius on unit shear capacity. Int. J. Geotech. Eng. 5, 463–467. https://doi.org/10.3328/IJGE.2011.05.04.463-467.

Smethurst, J.A., Clarke, D., Powrie, W., 2012. Factors controlling the seasonal variation in soil water content and pore water pressures within a lightly vegetated clay slope. Géotechnique 62, 429–446. https://doi.org/10.1680/geot.10.P.097.

Stokes, A., Atger, C., Bengough, A.G., et al., 2009. Desirable Plant root traits for protecting natural and engineered slopes against landslides. Plant and Soil 324, 1–30. https://doi.org/10.1007/s11104-009-0159-y.

Toyosawa, Y., Itoh, K., Kikkawa, N., et al., 2013. Influence of model footing diameter and embedded depth on particle size effect in centrifugal bearing capacity tests. Soils Found. 53, 349–356. https://doi.org/10.1016/j.sandf.2012.11.027.

White, D.J., Cheuk, C.Y., Bolton, M.D., 2008. The uplift resistance of pipes and plate anchors buried in sand. Géotechnique 58, 771–779. https://doi.org/10.1680/geot.2008.3692.

Wu, J., Kouretzis, G., Suwal, L., 2021. Bearing capacity mechanisms for pipes buried in sand. Can. Geotech. J. 58, 834–847. https://doi.org/10.1139/cgj-2020-0109.

Zhang, X., Knappett, J., Leung, A., Liang, T., 2018. Physical modelling of soil-structure interaction of tree root systems under lateral loads. In: 9th International Conference on Physical Modelling in Geoetchnics. Taylor & Francis, pp. 481–486.

Zhang, X., Knappett, J.A., Leung, A.K., et al., 2020. Small-scale modelling of root-soil interaction of trees under lateral loads. Plant and Soil 456, 289–305. https://doi.org/10.1007/s11104-020-04636-8.

Zhang, X., Knappett, J.A., Leung, A.K., et al., 2023. Centrifuge modelling of root-soil interaction of laterally loaded trees under different loading conditions. Géotechnique 73, 766–780. https://doi.org/10.1680/jgeot.21.00088.